From Global to Regional Projections – Insights from CMIP6

4

Authors:
Aurel Florian Moise, Sandeep Sahany, Muhammad Eeqmal Hassim, Chen Chen, Xin Rong Chua, Venkatraman Prasanna, Gerald Lim, Pavan Harika Raavi, Fei Luo

METEOROLOGICAL SERVICE SINGAPORE
Centre for Climate Research Singapore

4.1 Introduction

Climate change is an existential threat to humans and other beings on Earth. Hence it needs to be strategically understood and responded to in order to effectively manage the various risks associated with it. There is increasing evidence of the risks associated with climate change, and countries globally, especially small island nations like Singapore, need reliable and actionable climate change information to be prepared well in advance to adapt to the multi-faceted risks due to climate change.

Every ~7 years, the Intergovernmental Panel on Climate Change (IPCC) publishes Assessment Reports (ARs) that provide information about the state of scientific, technical and socio-economic knowledge on climate change, its impacts and future risks, and options for reducing the rate at which climate change is taking place. The IPCC, in its latest and sixth assessment cycle, produced the Working Group-I (WG-I) report on the Physical Science Basis (released on 09 August 2021), the WG-II report on Impacts, Adaptation and Vulnerability (released on 28 February, 2022), the WG-III report on Mitigation of Climate Change (released on 4 April, 2022), and finally the Synthesis Report (released on 20 March, 2023). The IPCC also produces Special Reports intermittently. Also, for the first time, as a part of the sixth assessment cycle, IPCC came up with the Climate Change Atlas which provides climate change information regionally. Although these reports are very useful to be informed on the global and large-scale climate change, since they are produced based on the literature that primarily comes from the climate change projections that comes from global climate models, they lack enough granularity to assess climate change at regional/local level and use the information for adaptation planning. Hence, as a follow up on Singapore's Second National Climate Change Study (V2), Singapore's Third National Climate Change Study (V3) aims to provide high resolution climate change projections for Singapore and the larger SEA region, by dynamically downscaling the coarse resolution global model data, that can be readily used for adaptation planning and thus help safeguard Singapore from the adverse effects of climate change.

The Third National Climate Change Study (V3) was commissioned by the National Environment Agency (NEA) under the Resilience Working Group (RWG) that studies Singapore's vulnerability to the effects of climate change and develops long-term plans that ensure the nation's resilience to future environmental changes. The RWG, is one out of the 5 WGs, namely, the Long-Term Emissions and Mitigation Working Group (LWG), Resilience Working Group, Sustainability Working Group (SWG), Green Economy Working Group (GEWG) and Communications and Engagement Working Group (CEWG), overseen by the Executive Committee (Exco) of the Inter-Ministerial Committee on Climate Change (IMCCC). The scientific work on producing the high-resolution downscaled climate projections was undertaken by the Meteorological Service Singapore's Centre for Climate Research Singapore (CCRS).

4.2 Key differences between CMIP5 and CMIP6

Climate models are considered as key tools for scientists to understand the past and present climate, predict the weather and climate on timescales from hours through years, and project climate change for decades and centuries under various global warming scenarios developed by the socio-economic scientists. These models simulate the physics, chemistry and biology of the climate system, owing to their numerical and scientific complexity, require the most advanced supercomputers to carry out long-term simulations.

The development of climate models has been a work-in-progress for many decades now, with increased spatial resolution, more advanced physics, and more advanced numerical methods to optimally utilise the advances in supercomputers. With numerous institutions developing and running climate models, the opportunity arose to coordinate globally standardised experiments using these models in order to find answers to specific science questions, especially on future climate change. This is where the Coupled Model Intercomparison Project (CMIP; https://www.wcrp-climate.org/

wgcm-cmip) comes in. CMIP is a framework for climate model experiments, allowing scientists to analyse, validate and improve GCMs in a systematic way. The “coupled” term in the name means that all the climate models in the project are atmosphere-land-ocean-sea ice components coupled GCMs. The word “intercomparison” is also important, as these coupled models are run in the same way as prescribed in the CMIP protocols so that the differences in model simulations can be directly attributed to the differences in the models and not to the differences in the way they are run (https://www.carbonbrief.org/qa -how- do -climate-models-work/#cmip).

CMIP started in 1995 and has been through several cycles to date. It comes under the purview of the Working Group on Coupled Modelling committee, which is part of the World Climate Research Programme (WCRP) based at the World Meteorological Organization (WMO) in Geneva. Literature produced in the form of peer-reviewed publications using the model simulations of CMIP has formed the basis for the IPCC assessment reports since the last couple of decades. The latest CMIP cycle that concluded around 2019 is called CMIP6 and provided most of the simulations that underpin the climate science assessed in the latest IPCC AR6 reports.

According to Eyring et al. (2016), with the Grand Science Challenges of the World Climate Research Programme (WCRP) as its scientific backdrop, CMIP6 aims to contribute to addressing three broad important science questions:

1. How does the Earth system respond to forcing?
2. What are the origins and consequences of systematic model biases?
3. How can we assess future climate changes given internal climate variability, predictability, and uncertainties in scenarios?

In the following subsections we discuss in more detail the three key differences between the CMIP5 and CMIP6 models relating to the equilibrium climate sensitivity in the two sets of models, shared socioeconomic pathways (future forcing scenarios used in the CMIP6 Scenario Model Intercomparison Project [ScenarioMIP]) and the key differences in the modelling systems used for simulations in the two generations of CMIP.

4.2.1 Equilibrium Climate Sensitivity (ECS)

The Equilibrium Climate Sensitivity (ECS) is defined as the global- and annual-mean near-surface air temperature rise that is expected to occur eventually, once all the excess heat trapped (top-of-atmosphere radiative imbalance) by the doubling of CO2 concentration relative to pre-industrial levels has been distributed evenly down into the deep ocean (i.e. when both the atmosphere and ocean have reached equilibrium with one another - a coupled equilibrium state). Many CMIP6 models exhibit an ECS of 5°C or higher (Zelinka et al., 2020), much higher than the upper value of the CMIP5 range of 4.5°C. Historically, the ECS range reported in CMIP has not shown much variation. The IPCC First Assessment Report (FAR) in 1990 estimated an ECS of 1.5 – 4.5°C, and the Second and Third Assessment Reports in 1996 and 2001 both were consistent with the ECS range reported in FAR. In AR4 the lower bond increased to 2.0°C from the earlier 1.5°C, but in AR5 this reverted back to the original range. All of these IPCC reports have been largely consistent with the 1979 US National Academies of Sciences Charney Report - the first comprehensive global assessment of climate change — which estimated ECS at the range of 1.5 – 4.5°C.

Given the ECS values have been increasing in many of the CMIP6 GCMs, in the Sixth Assessment Report (AR6), the IPCC narrowed down the Likely Range for ECS based on different approaches and considered evidence from multiple independent sources such as instrumental records, paleoclimate proxies, physical principles and also climate models (Sherwood et al., 2020).

Based on the analysis of Sherwood et al. (2020), the IPCC adopted the approach of employing an emulator for constraining temperature and all parameters scaling with temperature. Therefore, the IPCC reported uncertainty envelope has been significantly reduced (see also Chapter 11). This

is one of the key achievements in AR6 which has not been widely appreciated, but the efforts on narrowing the uncertainty of the range of model response to standard CO2 doubling has been long-standing and only in AR6 we see a significant narrowing.

The Likely Range now ranges between 2.5 - 4.0°C, down from what was reported in AR5. The IPCC also narrowed the Very Likely Range of ECS to be between 2.0 to 5.0°C, down from 1.0 to 6.0°C (Table 4.1).

Table 4.1: The Equilibrium Climate Sensitivity (ECS) ranges, as assessed by the IPCC in AR6, compared with the corresponding ranges reported in AR5

IPCC ECS Assessment	**AR6**	AR5
Likely Range	**2.5 to 4.0 K**	1.5 to 4.5 K
Very Likely Range	**2.0 to 5.0 K**	1.0 to 6.0 K

4.2.2 Shared Socioeconomic Pathways (SSPs)

A major difference between CMIP5 and CMIP6 is the future global warming scenarios used for climate change projections. The CMIP5 used four representative concentration pathways (RCPs), namely, RCPs 2.6, 4.5, 6.0, and 8.5, defined according to the radiative forcing levels reached by 2100 but did not include any socioeconomic storyline to go alongside them.

However, CMIP6 uses scenarios rooted in the socioeconomic trajectories that lead to corresponding radiative forcing levels, termed as Shared Socioeconomic Pathways (SSPs) (O'Neill et al., 2016). The four Tier-I (key scenarios to be used in various MIPs endorsed by CMIP6) scenarios include SSP1-2.6, SSP2-4.5, SSP3-7.0, and SSP5-8.5 (see Section 4.3 for more details). These SSPs were created, with varying assumptions about human developments including: population, urbanization, economic growth, technological developments, greenhouse gas and aerosol emissions, energy supply and demand, land-use changes, etc. The SSPs represent alternative storylines about how the world might develop over the coming century according to different climate policies, mitigation or adaptation responses.

There is a mapping between the SSPs and the corresponding RCPs used in CMIP5. The SSPs are mapped with the corresponding radiative forcing they are compatible with. For example, the SSP1 socioeconomic storyline cannot lead to 8.5W/m2 of radiative forcing in 2100, whereas SSP5 can. Hence SSP5-8.5 is a feasible scenario while SSP1-8.5 is not.

4.2.3 Models

The CMIP6 model archive consists of models at higher spatial resolution, more advanced physical parameterizations, and more earth system models with carbon cycle and biogeochemistry. The number of modelling groups participating in CMIP6 has also significantly gone up (49) as compared to 28 in CMIP5. This resulted in many separate models (>100) with different modelling centers contributing with more than one global climate model. In CMIP5 this number was less than half. Note that not all the different models contribute to all the various experiments, e.g. for the ScenarioMIP we saw only 49 models. This is because CMIP6 is made up of 20+ MIPs (Eyring et al., 2016), all addressing different research questions.

While many of the modelling centres have also increased the spatial resolution of their models in CMIP6 as compared to CMIP5, a few still have kept it the same. For example, for the scenario experiments exploring the evolution of future climate in response to changing greenhouse gas (GHG) emissions, the French model IPSL-CM5-LR (used in CMIP5) had a resolution of 1.9° latitude x 3.75° longitude, whereas the latest

version of this model (IPSL-CM6A-LR) used in CMIP6 has a resolution of 1.25° latitude x 2.5° longitude. On the other hand, CanESM2 (CMIP5) and CanESM5 (CMIP6) from the Canadian Centre for Climate Modelling and Analysis (CCCma) both have the same spatial resolution of 2.8° latitude x 2.8° longitude. Please see more model information in Table 5.1, and discussions on model independence in Chapter 5 section 5.5 (Table 5.3).

4.3 Future Climate Scenarios

According to Eyring et al. (2016), a set of common experiments within the CMIP6 called DECK (Diagnostic, Evaluation and Characterization of Klima) and the CMIP historical simulations (1850–near present) will maintain continuity and help document basic characteristics of models across different phases of CMIP. This was a key element of the CMIP6 design.

DECK: The DECK comprises four baseline experiments: (a) a historical Atmospheric Model Intercomparison Project (AMIP) simulation, (b) a pre-industrial control simulation (piControl), (c) a simulation forced by an abrupt quadrupling of CO2 (abrupt-4×CO2) and (d) a simulation forced by a 1 % yr−1 CO2 increase (1pctCO2). In addition to the DECK and historical simulations, there are 21 model intercomparison projects (MIPs) endorsed by CMIP6. ScenarioMIP is one of the key MIPs and the one that produces the simulations by forcing the GCMs with various future scenarios. Note that the AMIP experiments are atmosphere-only, coupled to land (but not ocean or sea ice) and that the latter are provided as boundary conditions.

Shared Socioeconomic Pathways (SSPs): The AR6 Report assesses the climate response to five global warming scenarios that cover the range of possible future development of climate change drivers found in the literature. The underlying model simulations come from ScenarioMIP mentioned above. The scenarios in the model simulations start in 2015 and are as follows:

(1) SSP1-1.9 - very low GHG emissions and CO2 emissions declining to net zero around or after 2050, followed by varying levels of net negative CO2 emissions,

(2) SSP1-2.6: low GHG emissions and CO2 emissions declining to net zero around or after 2050, followed by varying levels of net negative CO2 emissions,

(3) SSP2-4.5: intermediate GHG emissions and CO2 emissions remaining around current levels until the middle of the century,

(4) SSP3-7.0: high GHG emissions and CO2 emissions that roughly double from current levels by 2100, and

(5) SSP5-8.5: very high GHG emissions and CO2 emissions that roughly double from current levels by 2050, as illustrated in Figure 4.1. Emissions vary between scenarios depending on socio-economic assumptions, levels of climate change mitigation and air pollution controls.

Compared to CMIP5, the concept of SSPs expands on the framework of RCPs (Representative Concentration Pathways) by including various levels of socio-economic pathways (O'Neill et al., 2016)
.

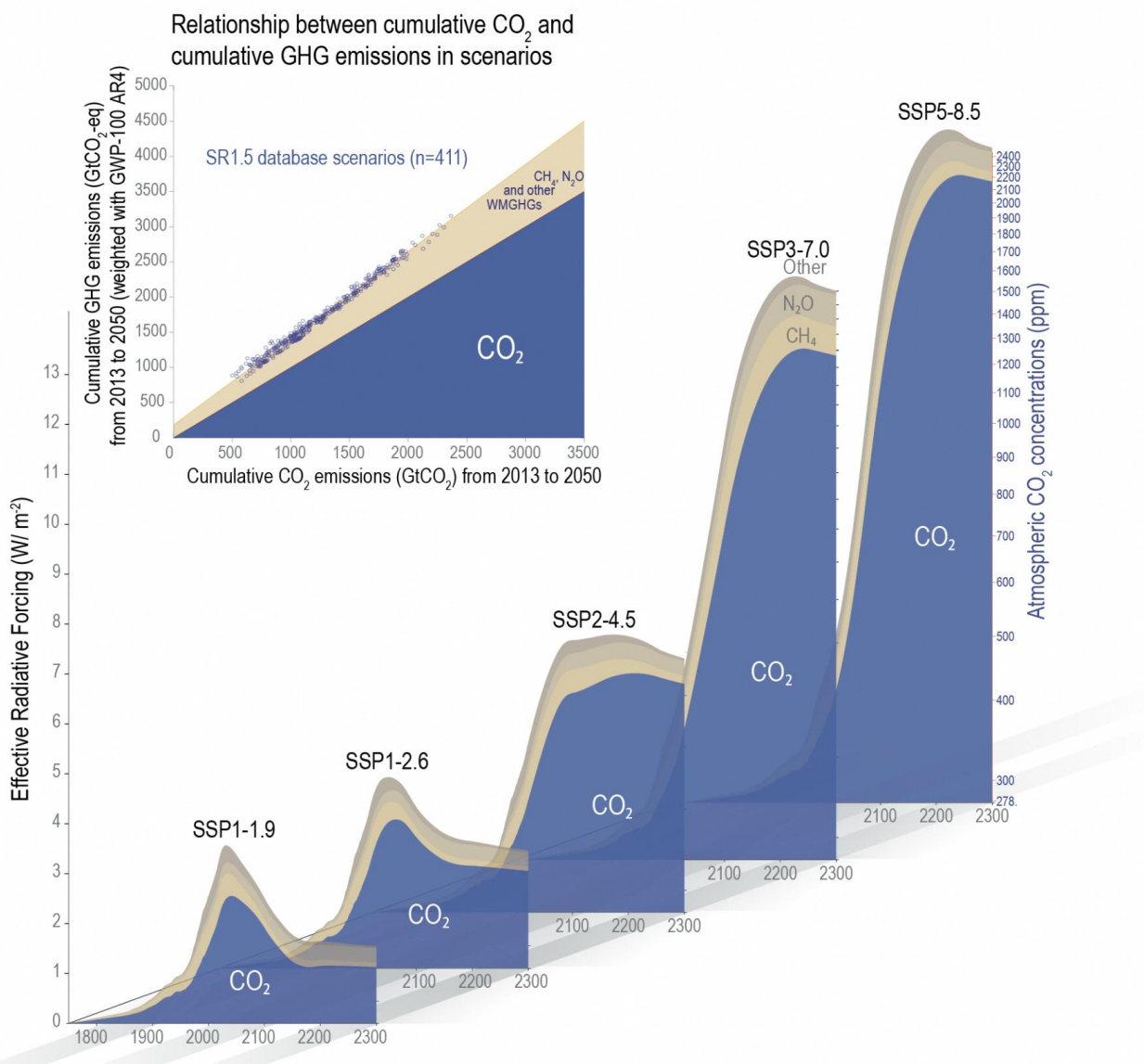

Figure 4.1: The role of CO_2 in driving future climate change in comparison to other greenhouse gases (GHGs). The GHGs included here are CH_4, N_2O, and 40 other long-lived, well-mixed GHGs. The blue shaded area indicates the approximate forcing exerted by CO_2 in Shared Socio-economic Pathways (SSP) scenarios, ranging from very low SSP1-1.9 to very high SSP5-8.5 (Chapter 7). The CO_2 concentrations under the SSP1-1.9 scenarios reach approximately 350 ppm after 2150, while those of SSP5-8.5 exceed 2000 ppm CO_2 in the longer term (up to year 2300). Similar to the dominant radiative forcing share at each point in time (lower area plots), cumulative GWP-100-weighted GHG emissions happen to be closely correlated with cumulative CO_2 emissions, allowing policymakers to make use of the carbon budget concept in a policy context with multi-gas GHG baskets as it exhibits relatively low variation across scenarios with similar cumulative emissions until 2050 (inset panel). (Figure 1.29 in IPCC, 2021: Chapter 1).

4.4 GCM-based global climate projections

In this section, we present the global climate projections reported in the IPCC AR6. Specifically, we present projected changes in global mean near-surface air temperature, rainfall, monsoon, ENSO, IOD, and MJO.

4.4.1 Temperature

The recent AR6 report states that the near-term (2021-2040) mean global surface air temperature

(GSAT) is extremely likely to increase by 0.4°C to 1.0°C relative to 1995 - 2014 with less dependence on the SSP scenario. However, the AR6 temperature projections using CMIP6 models predict an increase of 0.1°C to 0.2°C over the AR5 projections. In the near-term, the likelihood that the average GSAT would rise by 1.5°C relative to the 1850-1900 is higher in CMIP6 models under different scenarios due to improved methodology and continued global surface warming. The regional variations in surface temperatures indicate significant warming at higher latitudes, particularly during the Arctic's boreal winter. The highest rises in seasonal mean surface temperature under the SSP1-2.6 and SSP3-7.0 scenarios occur over land rather than oceans. In both scenarios, it is projected that seasonal mean surface temperatures of the Northern Hemisphere will increase by 1.0°C over the land regions.

The multi-model mean GSAT change (relative to 1850-1900; pre-industrial [PI]) from the CMIP6 GCMs with a higher ECS (>4°C) and those with medium ECS (2.5 °C <=T<=4°C) are shown in Figure 4.2. ECS values between 2.5 °C to 4°C are considered to be within the likely range as assessed by IPCC in AR6. Also shown are the observed anomalies from the same baseline using the Berkeley Earth dataset for the period 1850-2021. The historical anomalies are further merged with the projected change in GSAT for the high- and low-ECS models under the SSP5-8.5 scenario from 2015 to 2100.

The observed PI mean GSAT is found to be 13.8 °C. Both the high-ECS models and the medium-ECS models are found to underestimate the observed value (13.1°C in high-ECS models and 13.6°C in medium-ECS models). Notably, the high-ECS models simulate a cooler PI period as compared to the medium-ECS ones.

The observed anomalies for the period 1995-2014 (IPCC AR6 historical baseline period) from the PI were found to be 0.9°C. The corresponding anomalies for the high-ECS models during the same period were found to be the same as observed, and that for the medium-ECS models were lower than observed (0.7°C). Thus, even in the historical period the high-ECS models were warming at a higher rate.

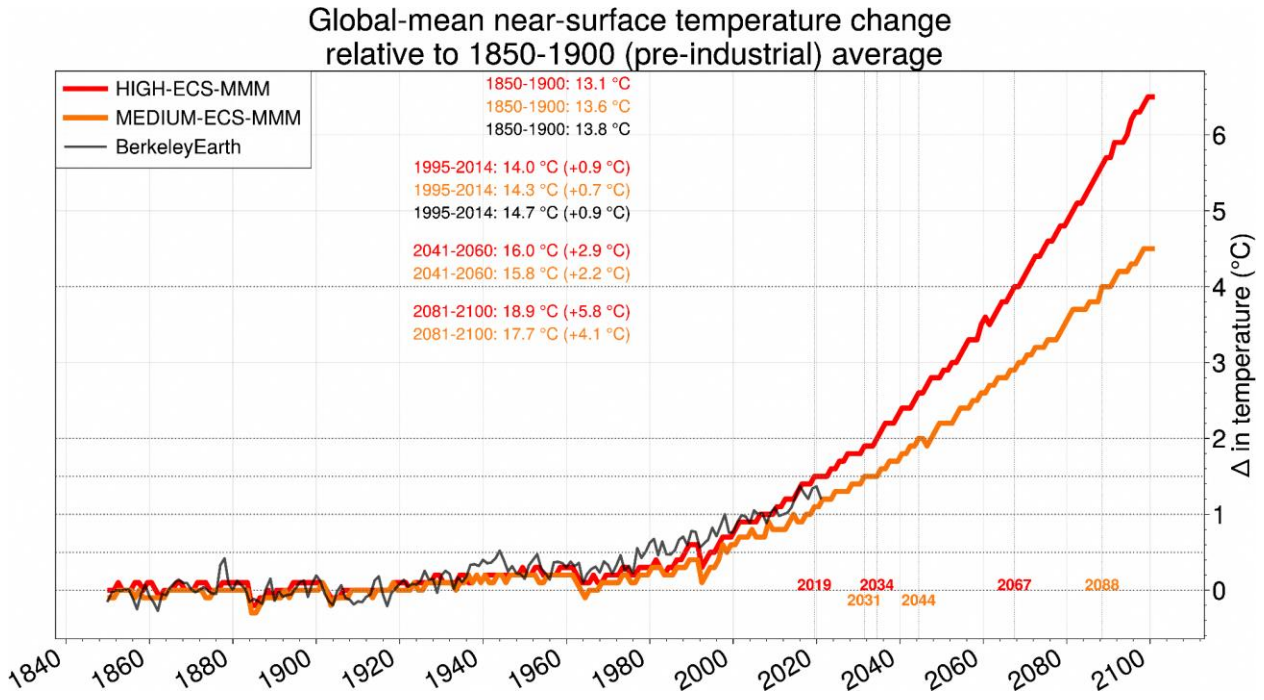

Figure 4.2: Time series of the multi-model mean (MMM) global average temperature anomaly from the HIGH-ECS (red line) and MEDIUM-ECS (orange line) model sets, respectively. Anomalies are relative to the 1850-1900 (pre-industrial) average. The observational time series is given by the Berkeley-Earth surface air temperature dataset (black line). The corresponding MMM

global average temperature for each dataset for the pre-industrial world (1850-1900), recent historical (1995-2014), mid-century (2041-2060) and end-century (2081-2100) periods are shown. Changes in the MMM global average temperature relative to the pre-industrial world in each dataset are shown in brackets. Coloured year values denote the first year in which the 1.5℃ and 2℃ global mean anomaly threshold is crossed in the HIGH- and MEDIUM-ECS models.

The projected mid-century (2041-2060) change for the high-ECS models was found to be 2.9°C and that for the medium-ECS models was found to be 2.2°C. By the end-century (2081-2100), the high-ECS models had warmed at an even faster rate and the multi-model mean projected change was found to be 5.8°C as compared to the corresponding change of 4.1°C projected by the medium-ECS models. Thus, the gap in the projected GSAT change between the high- and medium-ECS models kept increasing throughout the 21st century. The figure also shows that while the medium-ECS models will breach the 1.5°C global warming level (from PI) around 2031, the 2°C level around 2044, and the 4ºC level around 2088, the high-ECS models will reach the corresponding levels around 2019, 2034, and 2067, respectively. Note that the years mentioned above are based on annual mean values and not 20-year means and hence represent the first year when the corresponding warming level is reached.

4.4.2 Rainfall

According to the AR6 report, as the GSAT is projected to increase, there is an increased global land precipitation in the 21st century. At the end of the century (2081-2100), under the low emission scenario, the precipitation is projected to change by -0.2% to +4.7% and in the high emission scenario, the change is 0.9-12.9% relative to 1995-2014. More precipitation occurs at higher latitudes over oceans, wet tropical regions, and less over dry subtropics.

There are regional uncertainties and seasonal differences in the precipitation changes in the future warmer climate due to multiple reasons. Precipitation variations in the tropical oceans are mostly influenced by the changes in SST patterns, but in the subtropics, they are primarily influenced by the quick response to CO2 forcing (He & Soden, 2017). Natural and man-made aerosols have an impact on regional precipitation patterns in addition to their response to CO2 forcing (Shawki et al., 2018; Liu et al., 2018). The uncertainty in the precipitation estimates is attributed to model uncertainty, internal variability, and uncertainties in natural and anthropogenic aerosol emissions.

4.4.3 Monsoon

In CMIP6 models, under all future warming scenarios, the monsoon precipitation index, the area-weighted precipitation rate over the global monsoon land regions, is expected to rise due to increased moisture content (Chen et al., 2020). The CMIP6 projections indicate an increase in the global land monsoon precipitation by 1.3 -2.4 % per ºC of GSAT increase under different scenarios. In four of the five SSP scenarios, there is a tendency for the northern hemisphere summer monsoon circulation index (i.e., the vertical shear of zonal winds between 200 and 850 hPa averaged in an area 0-20N; 120W-120E) to decrease, potentially counteracting an increase in monsoon precipitation. Because of internal variability, including Atlantic Multi-decadal Variability (AMV) and Pacific Decadal Variability (PDV), the expected changes in the monsoon circulation are mainly uncertain.

The mid-century and end century projections indicate an asymmetry in monsoon rainfall with increased rainfall in the Northern Hemisphere than Southern Hemisphere, and an East-West asymmetry with enhanced Asian-African monsoon and weakened North American monsoon (Pascale et al., 2021; Wang et al., 2021). Overall, the global land monsoon precipitation is projected to increase despite reduced circulation under different scenarios in mid-century and end century. The combined contributions of model uncertainty and internal variability will have an impact on the projected changes in global monsoon precipitation and circulation.

4.4.4 ENSO

ENSO impacts precipitation variabilities worldwide (Ropelewski and Halpert 1987; Hendon

2003). Across the Indo-Pacific Ocean, ENSO induces a zonal dipole pattern of precipitation variability, i.e., positive variability in the tropical Pacific (TP) and “horseshoe” shaped negative variability towards the Maritime Continent (MC) (Langenbrunner and Neelin 2013). That is, TP becomes wetter than normal while MC becomes drier. Physically, ENSO-rainfall teleconnection over the MC is part of the ENSO-induced circulation responses over the tropics (Wang et al. 2003; Lau and Nath 2003; Stuecker et al. 2015). In boreal summer, when El Niño develops, a sequence of evolution begins with the eastward shifting of Walker Circulation due to the anomalous warming in the eastern Pacific. The shift suppresses convection over the MC (also weakens Asian–Australian Monsoon) and enhances convection in the Central Pacific.

Under warming, ENSO responses are uncertain across various emission scenarios and idealized simulations (Chen et al. 2017; Callahan et al. 2021; Cai et al. 2021; Brown et al. 2020). Tropical surface temperature variability changes are complex given oceanic and atmospheric processes, and the net effect of diverging feedbacks could potentially give less robust changes to the surface temperature variability and a low model agreement. On the contrary, the ENSO-induced precipitation variability over the TP strengthens robustly. It involves mean state changes beyond the bonds by ENSO itself, e.g. the tropical rainfall variability is strongly related to mean atmospheric changes associated with Clausius–Clapeyron relationship (Hu et al. 2021).

CMIP3 and CMIP5 models robustly projected that over the central-eastern Pacific the ENSO-induced rainfall variability strengthens (Bonfils et al. 2015; Perry et al. 2017; Yeh et al. 2018; Power et al. 2013; Kug et al. 2010; Chung and Power 2014; Chung et al. 2014; Chung and Power 2016, 2015). Besides the intensification, CMIP3 and CMIP5 models robustly project that, over the TP, ENSO-induced rainfall variability shifts eastward under warming (Yeh et al. 2018; Taschetto et al. 2020; Yan et al. 2020; Coelho and Goddard 2009; Huang and Xie 2015; Bayr et al. 2014; Kug et al. 2010; Power et al. 2013).

4.4.5 IOD

The mean climate state projections of the tropical Indian Ocean sea surface temperatures resemble the positive phase of the IOD mode with rapid warming in the west compared to the east. With no discernible change in frequency, these mean state modifications result in decreased amplitude differences between positive and negative IOD events. (Cai et al., 2013). However, these projected mean state changes might be due to biases of the model simulated current climate (Li et.al., 2016). Cai et al., (2021) showed an increased frequency of strong positive IOD events and a reduced frequency of moderate positive IOD events using the CMIP5 RCP8.5 and CMIP6 SSP5-8.5 simulations. These IOD projections indeed may depend on the realistic simulations of the background mean state changes of the Indian Ocean (Li et al., 2016). Hence, the future projections of IOD changes in the mid-term and long term remain uncertain due to lack of robust evidence and its reliance on the model's mean state biases.

4.4.6 MJO

According to sensitivity studies, MJO precipitation is expected to rise in magnitude with up to 14% per degree increases in warming (Adames et al., 2017; Wolding et al., 2017). In comparison to the CMIP3 or CMIP5 models, the CMIP6 models are significantly better at simulating the MJO. Reduced dry moisture bias in mean states results in improved and eastward propagation of the MJO over the MC (Ahn et al., 2020). Additionally, the amplitudes of MJO precipitation and zonal winds can now be reliably simulated in CMIP6 models (Orbe et al., 2020), and the model spread of the MJO characteristics has decreased (Chen et al., 2022). A multi-model mean of CMIP6 models shows a 17% increase in amplitude of precipitation, a 9% increase in MJO propagation speed, a 2-day reduction in MJO period, and a 5-degree eastward extension (Wang et al., 2023). The MJO is projected to become more intense under a warmer environment in the future, along with an increase in the associated precipitation amplitude.

4.5 GCM-based regional climate projections

In this section, we present the regional climate projections over the Southeast Asia/Maritime Continent region from our in-house analysis and relevant literature from the IPCC AR6 regional fact sheet for Asia. These regional climate projections are constructed based on the global climate models. Specifically, we present a summary of key climate change information over SEA from the IPCC AR6 regional fact sheet for Asia, projected changes in precipitation, projected changes in temperature, projected changes in ENSO teleconnections, and finally, projected changes in northeast monsoon surges.

Although one may still be able to derive some useful high-level information (for example, related to large-scale climate drivers such as ENSO) on regional climate change from GCM data, it is to be noted that the GCMs, due to their coarse spatial resolution, and also the complex topography and coastlines of the Maritime Continent are unable to accurately represent small islands such as Singapore in the model. For example, while one GCM may "see" Singapore as a part of peninsular Malaysia, another GCM may "see" it as an ocean point. This is precisely the reason why high-resolution regional climate change projections such as V3 need to be carried out, so that the finer spatial scale information can be produced, both for more reliable physical climate change assessment and for conducting downstream high-resolution impact studies.

4.5.1 Summary of SEA Projections from the IPCC AR6 Climate Atlas

As one of the outreach products, the IPCC AR6 constructed regional fact sheets by dividing the world into 11 regions and collating key climate change messages for each of these regions. These regions are further divided into subregions. The fact sheets constitute an entry point for regionalized information in the Chapters, the Technical Summary and the Interactive Atlas. The Asian region and its various subregions are shown in Figure 4.3. The Southeast Asian subregion is marked as "SEA" in the figure.

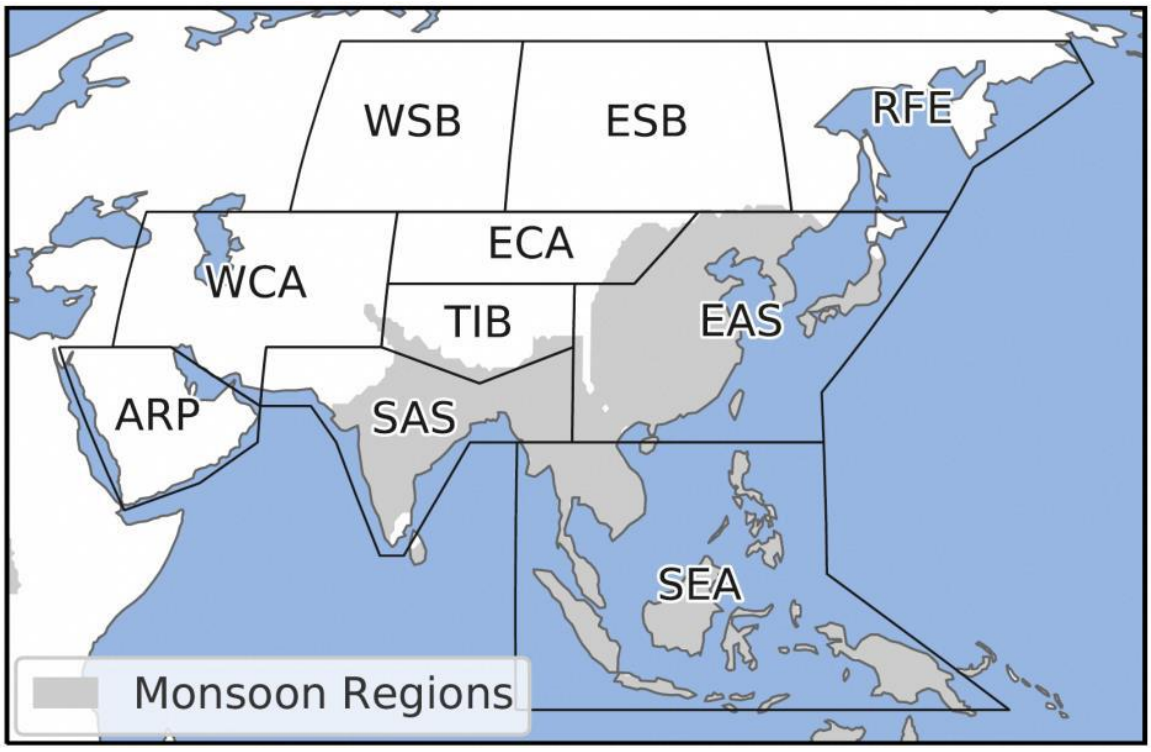

Figure 4.3: The various subregions of Asia for which climate change information has been provided in the regional factsheet. Also shown in grey are the monsoon regions. (Map from the Regional fact sheet for Asia, IPCC).

Key messages for the SEA subregion are presented below, along with the associated confidence levels (where available) assessed by the IPCC:

1. Future warming over SEA will be slightly less than the global average (high confidence).
2. Rainfall will increase in the northern parts of mainland SEA and decrease in the Maritime Continent in some seasons (medium confidence).
3. In the near-term, South and Southeast Asian monsoon and East Asian summer monsoon precipitation changes will be dominated by the effects of internal variability (medium confidence).
4. Compound impacts of climate change, land subsidence, and local human activities will lead to higher flood levels and prolonged inundation in the Mekong Delta (high confidence).

4.5.2 Precipitation Changes over SEA from CMIP6 GCMs

The mean multi-model changes in the annual mean and seasonally-averaged rainfall for the end-century 2081-2100 period are shown in Figure 4.4 for all available CMIP6 models. Also shown are the mean changes found in the subset of models with high ECS (ECS > 4 K) and those with medium climate sensitivity (2.5 ≤ ECS ≤ 4 K).

On the annual time scale, precipitation is likely to increase overall land areas. The biggest changes are projected over the northern (mainland) SEA region and over Borneo and New Guinea. In contrast, decreases are seen over large portions of water. Also note that Singapore lies in between wider areas of projected rainfall increase and projected rainfall decrease in most of the season, making rainfall projections for Singapore particularly challenging. The magnitude of projected changes in mean annual rainfall appears largely similar between high and medium ECS models, except in the easternmost portion of the domain (equatorial western Pacific), where the high ECS models show a larger magnitude.

A different story emerges between the two subsets of high ECS and medium ECS models. For seasons other than the northern hemisphere winter (DJF), the spatial pattern of changes is largely coherent between the high and medium ECS models. However, the high ECS models (Figure 4.4 e,h,k,n) project much stronger changes in mean seasonal rainfall over many land and water areas than the medium ECS models (Figure 4.4 f,i,l,o). This suggests that the regional precipitation response tends to scale with the level of warming. Most notable are the strong drying signals projected for vast areas north (south) of the equator in MAM (JJA).

The spatial pattern of these signals largely resembles the historically known mean response to El Niño events. They are, therefore, most likely associated with the projected emergence of more El Niño-like conditions in the future (e.g. Cai et al., 2014, 2021) and the enhanced and eastward shift of the ENSO-rainfall teleconnection over the region (Chen et al. 2023; see also Sec 4.5.4). Interestingly, the full ensemble signals for MAM, JJA and SON in Figure 4.4 g, j, m, appear to be mainly driven by changes projected by the high ECS models.

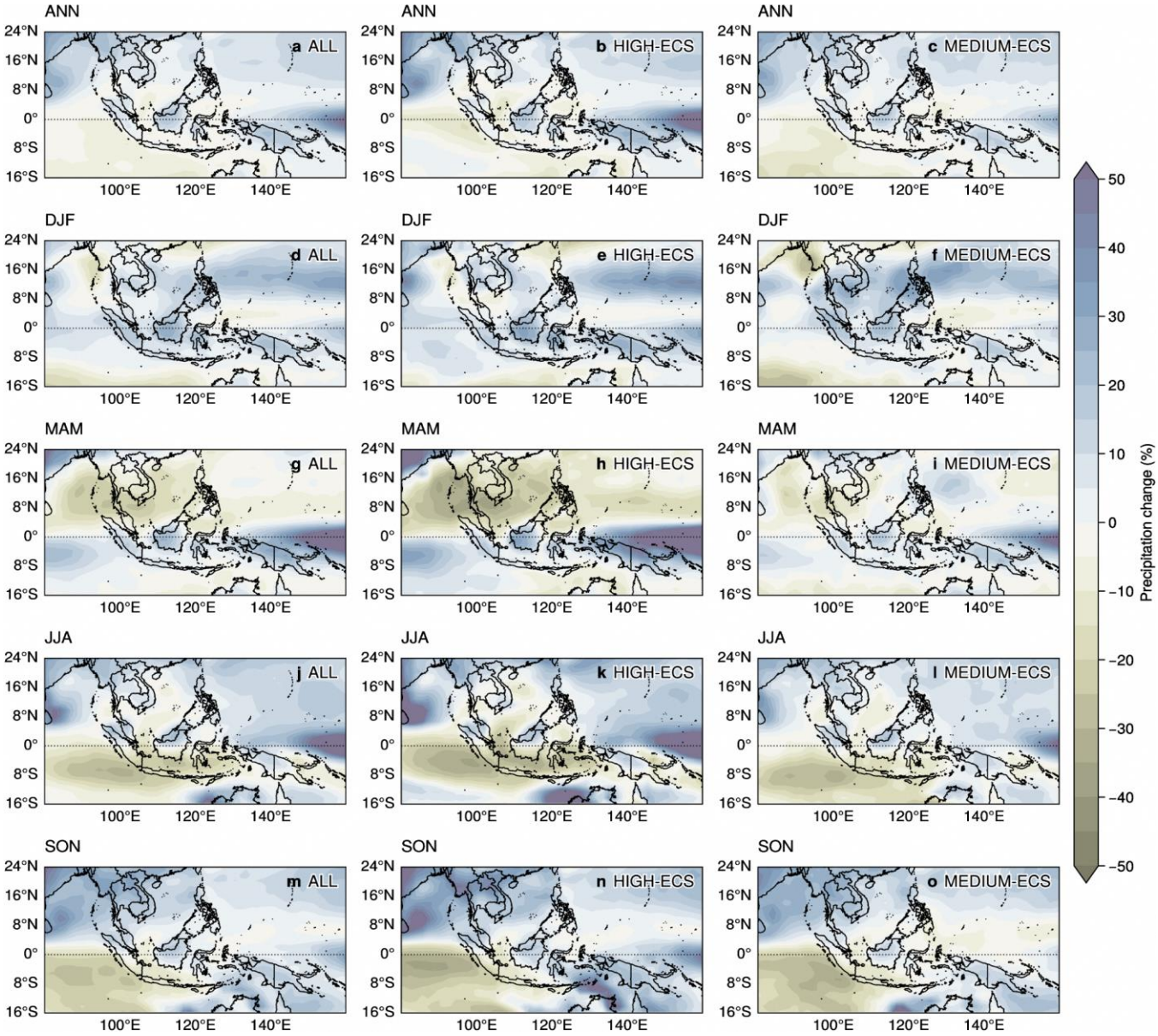

Figure 4.4: Mean multi-model changes in precipitation (in %) for end-century (2081-2100) under the SSP5-8.5 scenario for CMIP6 GCMs that have both future and historical periods available. Each column shows the set of ALL CMIP6 (n=36), HIGH-ECS (n=13) and MEDIUM-ECS (n=13) models, respectively, and each row shows the season. (a-c) Annual (ANN) changes. (d-f) December-February (DJF) changes. (g-i) March-May (MAM) changes. (j-l) June-August (JJA) changes. (m-o) September-November (SON) changes.

4.5.3 Temperature Changes over SEA from CMIP6 GCMs

Changes in daily mean temperature across the SEA domain are shown in Figure 4.5. As expected, the high ECS models project much higher daily mean temperature changes over both land and sea and also stronger land-sea contrasts on the annual and seasonal time scales (Fig. 4.5 b, e, h, k, n). Changes in excess of 5^{o}C are even projected in the hotter summer periods of the year in MAM and JJA, particularly in the interior northern portions of mainland SEA. Differences in the projected temperature changes between the high and medium ECS models amount to at least 1^{o}C over sea and up to around 2^{o}C over land. Furthermore, similar magnitudes of temperature change are projected regardless of season within

each group of models, suggesting that global warming affects all seasons equally.

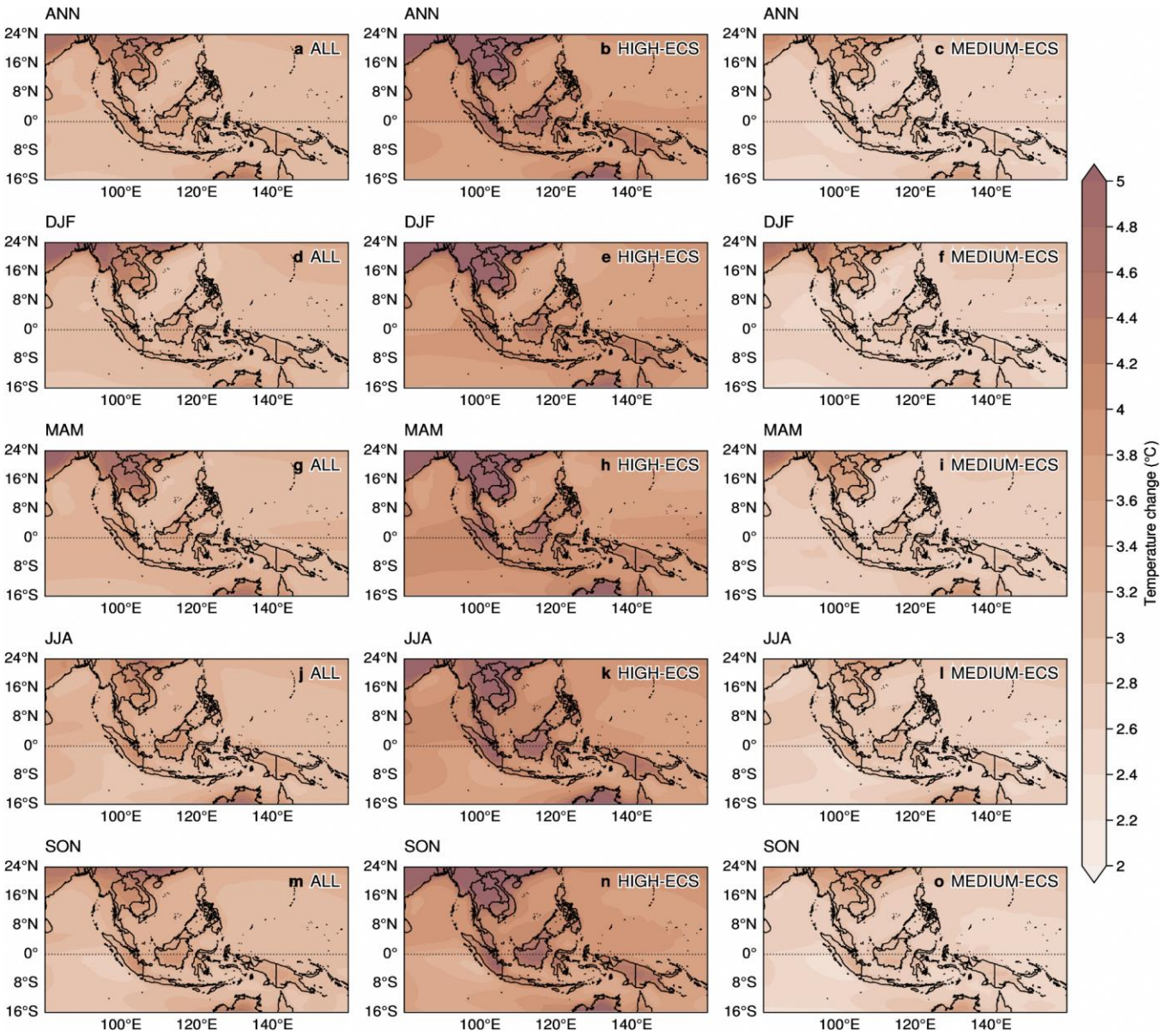

Figure 4.5: As in Fig. 4.4 but for mean multi-model changes in daily average temperature (in °C).

4.5.4 ENSO teleconnection changes under warming

The Maritime Continent (MC), located in the heart of the Indo-Pacific warm pool, plays an important role in the global climate. However, the future MC climate is largely unknown, in particular the ENSO-rainfall teleconnection (Fig. 4.6 & Fig. 4.9). ENSO induces a zonal dipole pattern of rainfall variability across the Indo-Pacific Ocean, i.e., positive variability in the Tropical Pacific and negative variability towards the MC. Here, new CMIP6 models robustly project that, for both land and sea rainfall, the negative ENSO teleconnection over the MC (drier/wetter during El Niño/La Niña) could intensify significantly under the SSP585 warming scenarios (Fig. 4.7). Strengthened teleconnection may cause

enhanced droughts and flooding, leading to agricultural impacts and altering rainfall predictability over the region. Models also project that the Indo-Pacific rainfall center and the zero-crossing of dipole-like rainfall variability both shift eastward, which adjustments are more notable during boreal summer than winter (Fig. 4.8). All these projections are robustly supported by the model agreement and scale up with the warming trend.

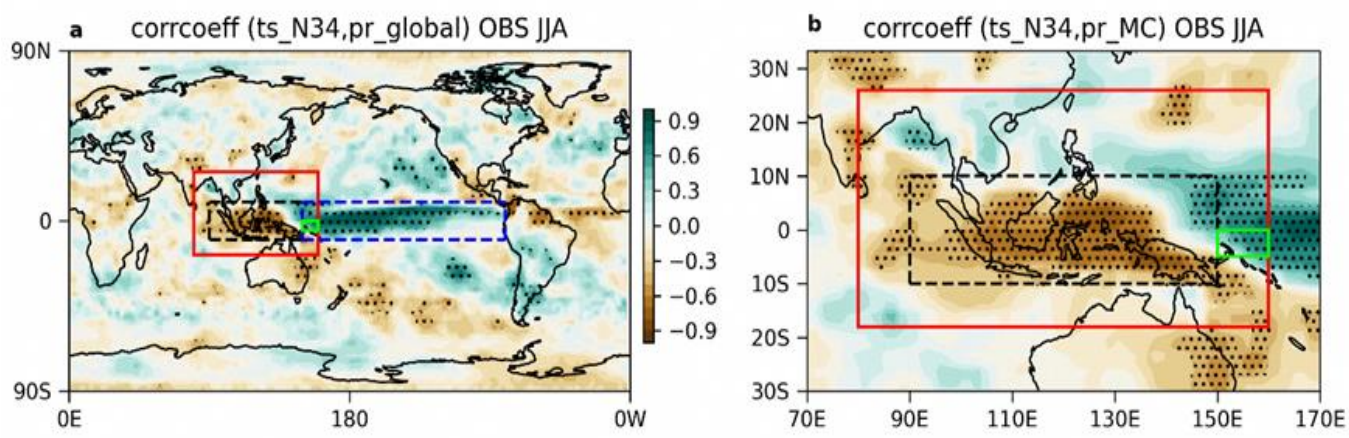

Figure 4.6: Observed ENSO-rainfall teleconnection. a. Observed global ENSO-precipitation correlation coefficient during boreal summer (JJA). Here the correlation coefficient is calculated between the anomalous precipitation (pr) and Niño3.4 sea surface temperature (ts). Stipping area indicates significant correlation with p-value<0.01. Defined domains of Maritime Continent (MC) (red box), Central Maritime Continent (CMC) (black dashed box), Eastern Maritime Continent (EMC) (green box), and tropical Pacific (TP)(blue dashed box) are shown. b. similar to a, but focusing on the MC.

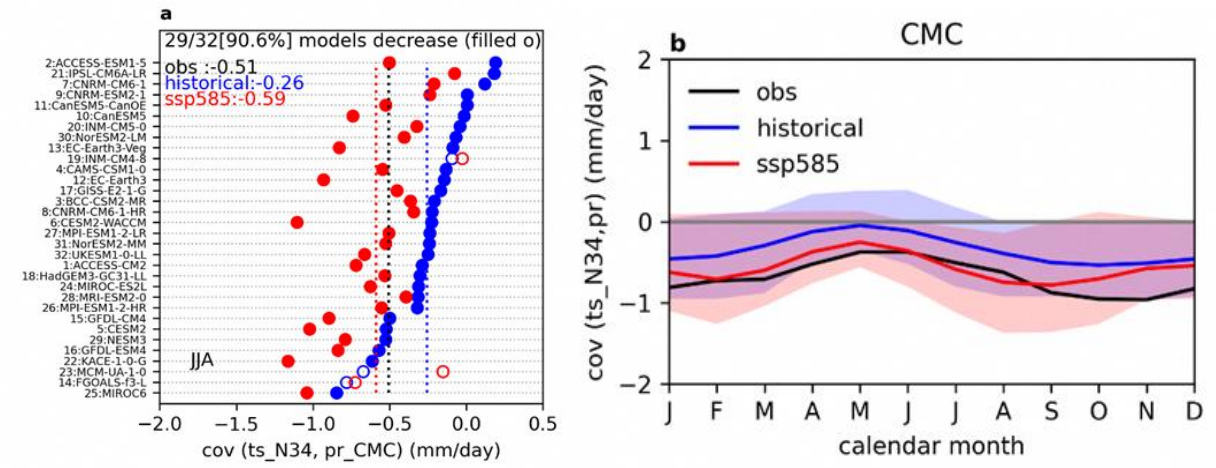

Figure 4.7: Summer (JJA) ENSO-rainfall teleconnection in the CMC is enhanced under warming. a. ENSO-precipitation covariance for the CMC domain across 32 CMIP6 models. The observation (black line), the model mean for the historical period (blue line), and the model mean for the future SSP585 scenario (red line) are shown. Model results are ranked by their values in the historical period. Model agreement on the future change is shown on the top. b. 12-month ENSO-precipitation covariance across the CMC. Observations (GPCP, black curve), the multi-model mean of 32 CMIP6 models for the historical period (blue curve), and the multi-model mean for the SSP585 scenario (red curve) are shown. The shades indicate the 95% model range.

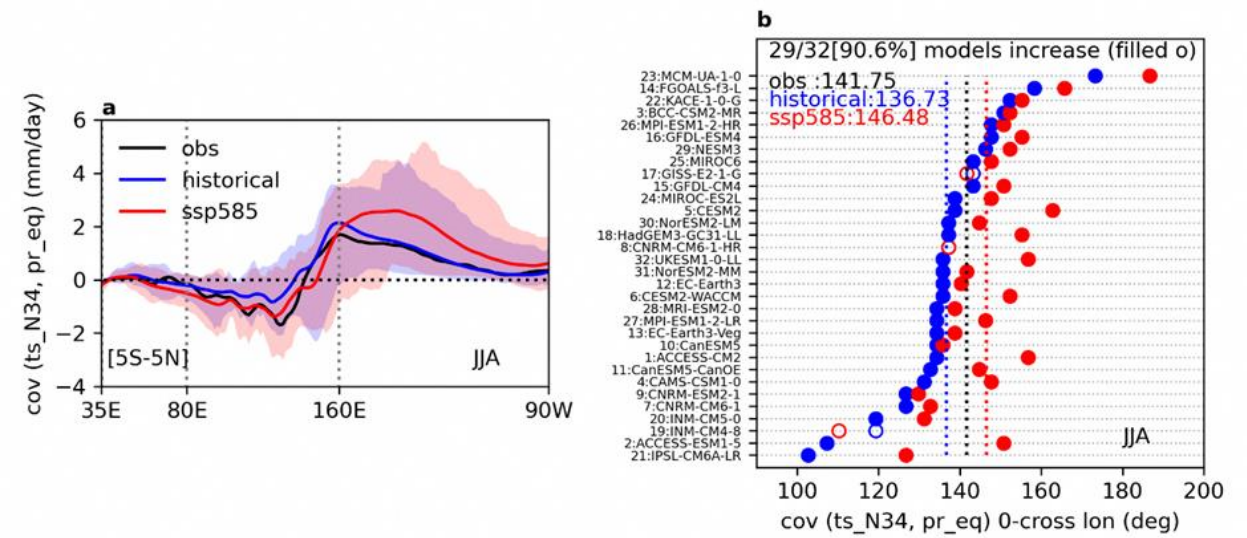

Figure 4.8: Summer (JJA) zonal dipole-like ENSO-rainfall teleconnection shifts eastward under warming. a. Equatorial precipitation [5S-5N averaged] covariance with Niño3.4 sea surface temperature. Observations (GPCP, black curve), the multi-model mean of 32 CMIP6 models for the historical period (blue curve), and the multi-model mean for the SSP585 scenario (red curve) are shown. The shades indicate the 95% model range. b. Zero-crossing longitude of the precipitation covariance across 32 CMIP6 models. The observation (black line), the model mean for the historical period (blue line), and the model mean for the future SSP585 scenario (red line) are shown. Model results are ordered by their values in the historical period. Model agreement on the future change is shown on the top.

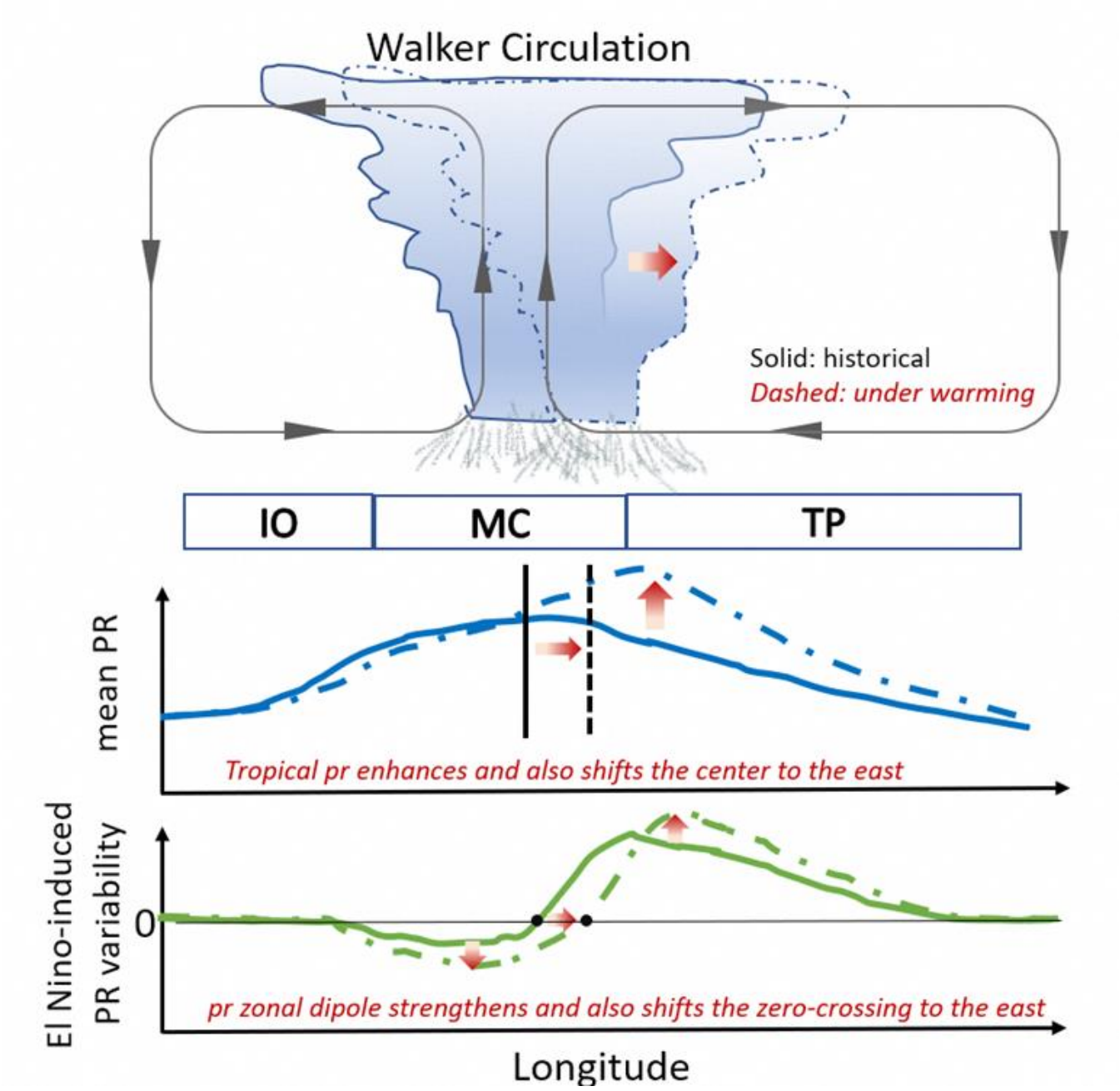

Figure 4.9: Schematic diagram showing the physical relationship between future changes in rainfall and ENSO-rainfall teleconnection. Across the longitude, the left is the Indian Ocean (IO), the middle is the Maritime Continent (MC), and the right is the Tropical Pacific (TP). Under warming, the deep convection center above the warm pool and the Walker Circulation shifts eastward. The first row shows that tropical precipitation enhances but also shifts the center to the east. The second row shows that ENSO-induced precipitation variability displays a zonal dipole structure (positive in the TP and negative in the MC), and this dipole strengthens under warming and shifts the zero-crossing longitude to the east.

4.5.5 Northeast Monsoon Surge changes under warming

Figure 4.10 shows the projected changes in rainfall and 850 hPa winds composited over northeast monsoon surge days using 6 GCMs. The definition of surge days follows in Chapter 3.7, where the mean and standard deviation are calculated separately for historical and SSP5-8.5. Rainfall increases are projected around Borneo,

Sulawesi, south Sumatra, New Guinea, and east of the Philippines, and drying around the Maluku Islands). The increase in surge rainfall over Borneo and New Guinea, together with the increase of DJF and SON rainfall over these two regions (Figure 4.4), suggests the surges could be related to changes in rainfall over those time periods. As for winds, the projected changes include easterlies over Indochina and west of Sumatra, as well as westerlies north of New Guinea. There is also an increase in surge frequency from 18% to 19%.

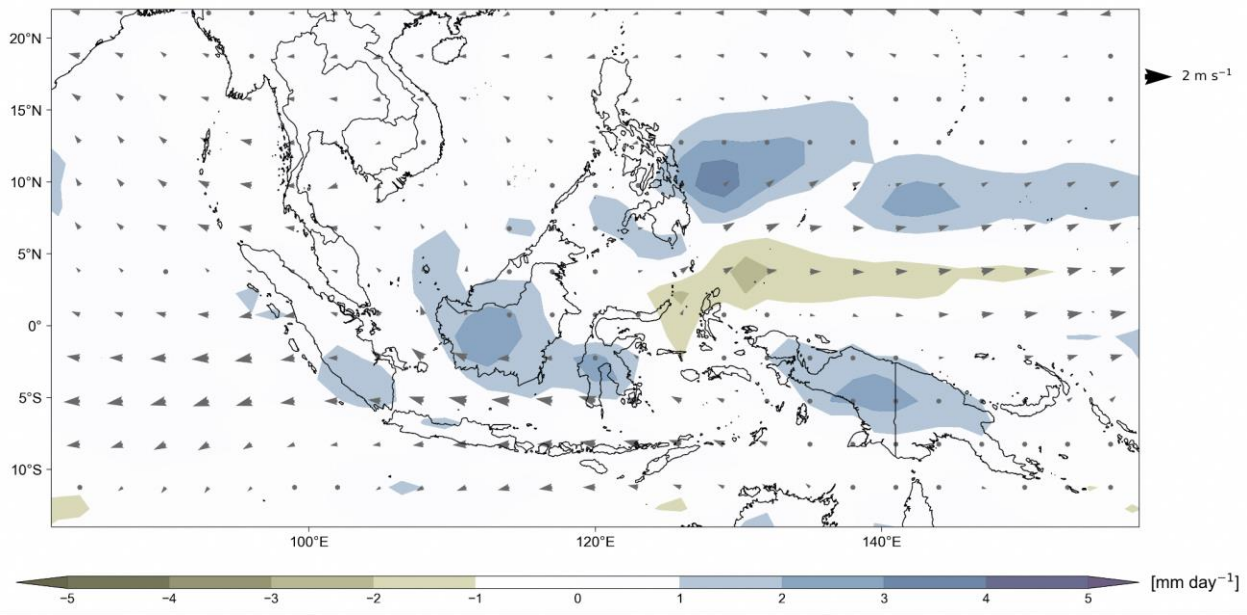

Figure 4.10: shows the change in 850 hPa wind direction (arrows) and rainfall (shaded) composited over surge days from 2080-2099 in SSP5-8.5 with respect to 1995-2014 in 6 GCMs, regridded to 1.5 x1.5 (those used for downscaling).

The results indicate that Singapore might experience more surge events, but that the magnitude of rainfall from these events as a whole might not change much. One caveat is that we have not examined how changes in the strongest monsoon surge events might change with warming, which has implications for the precipitation extremes experienced over Singapore (see Chapter 10.3 for further discussion).

4.6 Summary

The current chapter focuses on using Global and regional climate projections from the CMIP6 models (used in IPCC AR6) to comprehend information about climate change at global and regional scales. Here, we describe the projected changes in some important climate variables (i.e. temperature and rainfall), associated climate drivers (monsoon, ENSO, IOD, MJO), and regional teleconnections mainly influencing the Southeast Asian climate.

The CMIP6 models have higher spatial resolution, improved model physics (parameterization schemes), and more earth system models with carbon cycle and biogeochemistry compared to the CMIP5 models. The equilibrium climate sensitivity (ECS) values in many of the CMIP6 models are projected to be higher than the CMIP5 models. The CMIP6 models, compared to earlier CMIP5 models, also have a socioeconomic storyline (SSP1-2.6, SSP2-4.5, SSP3-7.0, and SSP5-8.5) along with radiative forcing levels (CMIP5 models; Representative Concentration Pathways (RCP) 2.6, 4.5, 6.0 & 8.5) for the future warming scenarios. Therefore, one may expect higher confidence in the future projections of different climate variables and processes using

the CMIP6 models compared to earlier CMIP5 models.

The global mean surface air temperature is projected to increase by 0.4 to 1.0^{o}C relative to 1995 - 2014 across most of the scenarios in the near term (2021-2040). Also, the land surface temperatures are expected to rise at least 1.0^{o}C higher than the oceans during the same period. The near-term land precipitation is expected to increase under both low emission (-0.2 to 4.7%) and high emission (0.9 to 12.9%) scenarios with certain regional uncertainties due to internal variability, model uncertainty, and uncertainties in aerosol emissions.

Under different warming scenarios, the global monsoon precipitation is expected to increase despite reduced circulation strength both in the mid and end century. The ENSO response due to warming is uncertain across different scenarios but has a strong signal of ENSO-induced precipitation variability over the tropical Pacific. Although the frequency of strong positive IOD is projected to increase, the IOD response is uncertain due to the lack of strong evidence and dependency on mean state biases of the model. In a future warmer climate, the MJO is projected to become more intense with an increased magnitude of associated precipitation.

The regional projections over the SEA region show that mean surface temperature increases across the SEA are slightly less than the global. The daily mean surface temperatures are expected to increase over land and oceans with stronger land-sea contrast in high ECS models at annual and seasonal time scales. The temperatures are expected to rise up to 5^{o}C during hot summer periods in MAM and JJA seasons over northern parts of SEA. The mean annual rainfall projections show increased values over most of the land regions of SEA, with higher increases over the northern SEA, Borneo, and New Guinea. The regional precipitation response across different seasons tends to scale with the level of warming, i.e. the high ECS models have stronger regional rainfall changes compared to the medium ECS models. In CMIP6 models, under the higher warming scenario (SSP5-8.5), there is a strong ENSO-rainfall signal over the MC with strong drier conditions during El Niño and strong wetter conditions during La Niña.

There is an increased frequency of Northeast monsoon surges to 19% (from the current 18%) with increased rainfall over Borneo, Sulawesi, south Sumatra, New Guinea, and east of the Philippines, and reduced rainfall around the Maluku islands. Due to the combined effects of climate change, land subsidence, and regional human activity, there is a higher degree of confidence in the increasing floods and prolonged inundation across the Mekong Delta region.

Overall, the CMIP6 future projections indicate increased global and regional surface air temperatures, enhanced global precipitation (regional differences; wet gets wetter, dry gets drier), increased monsoon land precipitation, and enhanced ENSO-rainfall teleconnections. In addition to the mean changes, extremes in temperature and rainfall are projected to increase, especially under SSP5-8.5 over many parts of the globe, including SEA.

References

Adames, Á.F., Kim, D., Sobel, A.H., Del Genio, A. and Wu, J., 2017. Characterization of moist processes associated with changes in the propagation of the MJO with increasing CO2. Journal of advances in modeling earth systems, 9(8), pp.2946-2967.

Ahn, M.S., Kim, D., Kang, D., Lee, J., Sperber, K.R., Gleckler, P.J., Jiang, X., Ham, Y.G. and Kim, H., 2020. MJO propagation across the Maritime Continent: Are CMIP6 models better than CMIP5 models? Geophysical Research Letters, 47(11), p.e2020GL087250.

Arnold, N.P. and Randall, D.A., 2015. Global-scale convective aggregation: Implications for the Madden-Julian Oscillation. Journal of Advances in Modeling Earth Systems, 7(4), pp.1499-1518.

Bayr, T., D. Dommenget, T. Martin, and S. B. Power, 2014: The eastward shift of the Walker Circulation in response to global warming and its relationship to ENSO variability. Clim. Dyn., 43, 2747–2763, https://doi.org/10.1007/s00382-014-2091-y.

Bonfils, C. J. W., B. D. Santer, T. J. Phillips, K. Marvel, L. Ruby Leung, C. Doutriaux, and A. Capotondi, 2015: Relative contributions of mean-state shifts and ENSO-driven variability to precipitation changes in a warming climate. J. Clim., 28, 9997–10013, https://doi.org/10.1175/JCLI-D-15-0341.1.

Brown, J., and Coauthors, 2020: Comparison of past and future simulations of ENSO in CMIP5/PMIP3 and CMIP6/PMIP4 models. Clim. Past Discuss., 1–44, https://doi.org/10.5194/cp-2019-155.

Chen, C., M. A. Cane, A. T. Wittenberg, and D. Chen, 2017: ENSO in the CMIP5 Simulations: Life Cycles, Diversity, and Responses to Climate Change. J. Clim., 30, 775–801, https://doi.org/10.1175/JCLI-D-15-0901.1.

Chen, G., Ling, J., Zhang, R., Xiao, Z. and Li, C., 2022. The MJO from CMIP5 to CMIP6: Perspectives from tracking MJO precipitation. Geophysical Research Letters, 49(1), p.e2021GL095241.

Callahan, C. W., C. Chen, M. Rugenstein, J. Bloch-Johnson, S. Yang, and E. J. Moyer, 2021: Robust decrease in El Niño/Southern Oscillation amplitude under long-term warming. Nat. Clim. Chang., 11, 752–757, https://doi.org/10.1038/s41558-021-01099-2.

Cai, W., Zheng, X.T., Weller, E., Collins, M., Cowan, T., Lengaigne, M., Yu, W. and Yamagata, T., 2013. Projected response of the Indian Ocean Dipole to greenhouse warming. Nature geoscience, 6(12), pp.999-1007.

Cai, W., Santoso, A., Wang, G., Weller, E., Wu, L., Ashok, K., Masumoto, Y. and Yamagata, T., 2014. Increased frequency of extreme Indian Ocean Dipole events due to greenhouse warming. Nature, 510(7504), pp.254-258.

Cai, W., Yang, K., Wu, L., Huang, G., Santoso, A., Ng, B., Wang, G. and Yamagata, T., 2021. Opposite response of strong and moderate positive Indian Ocean Dipole to global warming. Nature Climate Change, 11(1), pp.27-32.

Cai, W., and Coauthors, 2021: Changing El Niño–Southern Oscillation in a warming climate. Nat. Rev. Earth Environ., 2, 628–644, https://doi.org/10.1038/s43017-021-00199-z.

Chu, J.E., Ha, K.J., Lee, J.Y., Wang, B., Kim, B.H. and Chung, C.E., 2014. Future change of the Indian Ocean basin-wide and dipole modes in the CMIP5. Climate dynamics, 43, pp.535-551.

Chung, C. T. Y., and S. B. Power, 2014: Precipitation response to La Niña and global warming in the Indo-Pacific. Clim. Dyn., 43, 3293–3307, https://doi.org/10.1007/s00382-014-2105-9.

Chung, C. T. Y., S. B. Power, J. M. Arblaster, H. A. Rashid, and G. L. Roff, 2014: Nonlinear precipitation response to El Niño and global warming in the Indo-Pacific. Clim. Dyn., 42, 1837–1856, https://doi.org/10.1007/s00382-013-1892-8.

Chung, C. T. Y., and S. B. Power, 2015: Modelled rainfall response to strong El Niño sea surface temperature anomalies in the tropical pacific. J. Clim., 28, 3133–3151, https://doi.org/10.1175/JCLI-D-14-00610.1.

Chung, C. T. Y., and S. B. Power, 2016: Modelled impact of global warming on ENSO-driven precipitation changes in the tropical Pacific. Clim. Dyn., 47, 1303–1323, https://doi.org/10.1007/s00382-015-2902-9.

Coelho, C. A. S., and L. Goddard, 2009: El Niño-induced tropical droughts in climate change projections. J. Clim., 22, 6456–6476, https://doi.org/10.1175/2009JCLI3185.1.

Hendon, H. H., 2003: Indonesian Rainfall Variability: Impacts of ENSO and Local Air–Sea Interaction. J. Clim., 16, 1775–1790.

Hu, K., G. Huang, P. Huang, Y. Kosaka, and S.-P. Xie, 2021: Intensification of El Niño-induced atmospheric

anomalies under greenhouse warming. Nat. Geosci., https://doi.org/10.1038/s41561-021-00730-3.

Huang, P., and S.-P. Xie, 2015: Mechanisms of change in ENSO-induced tropical Pacific rainfall variability in a warming climate. Nat. Geosci., 1–13, https://doi.org/10.1038/ngeo2571.

Kikuchi, K., Wang, B. and Kajikawa, Y., 2012. Bimodal representation of the tropical intraseasonal oscillation. Climate Dynamics, 38, pp.1989-2000.

Kim, H., Vitart, F. and Waliser, D.E., 2018. Prediction of the Madden–Julian oscillation: A review. Journal of Climate, 31(23), pp.9425-9443.

Langenbrunner, B., and J. D. Neelin, 2013: Analyzing ENSO Teleconnections in CMIP Models as a Measure of Model Fidelity in Simulating Precipitation. J. Clim., 26, 4431–4446, https://doi.org/10.1175/JCLI-D-12-00542.1.

Lau, N. C., and M. J. Nath, 2003: Atmosphere-ocean variations in the Indo-Pacific sector during ENSO episodes. J. Clim., 16, 3–20.

Lee, J.Y., Wang, B., Wheeler, M.C., Fu, X., Waliser, D.E. and Kang, I.S., 2013. Real-time multivariate indices for the boreal summer intraseasonal oscillation over the Asian summer monsoon region. Climate Dynamics, 40, pp.493-509.

Li, G., Xie, S.P. and Du, Y., 2016. A robust but spurious pattern of climate change in model projections over the tropical Indian Ocean. Journal of Climate, 29(15), pp.5589-5608.

Kug, J. S., S. Il An, Y. G. Ham, and I. S. Kang, 2010: Changes in El Niño and La Niña teleconnections over North Pacific-America in the global warming simulations. Theor. Appl. Climatol., 100, 275–282, https://doi.org/10.1007/s00704-009-0183-0.

Madden, R.A., 1986. Seasonal variations of the 40-50 day oscillation in the tropics. Journal of Atmospheric Sciences, 43(24), pp.3138-3158.

Madden, R.A. and Julian, P.R., 1994. Observations of the 40–50-day tropical oscillation—A review. Monthly weather review, 122(5), pp.814-837.

Maloney, E.D., Adames, Á.F. and Bui, H.X., 2019. Madden–Julian oscillation changes under anthropogenic warming. Nature Climate Change, 9(1), pp.26-33.

Power, S., F. Delage, C. Chung, G. Kociuba, and K. Keay, 2013: Robust twenty-first-century projections of El Niño and related precipitation variability. Nature, 502, 541–545, https://doi.org/10.1038/nature12580.

Ropelewski, C. F., and M. S. Halpert, 1987: Global and Regional Scale Precipitation Patterns Associated with the El Niño/Southern Oscillation. Mon. Weather Rev., 115, 1606–1626, https://doi.org/10.1175/1520-0493(1987)115<1606:GARSPP>2.0.CO;2.

Roxy, M.K., Dasgupta, P., McPhaden, M.J., Suematsu, T., Zhang, C. and Kim, D., 2019. Twofold expansion of the Indo-Pacific warm pool warps the MJO life cycle. Nature, 575(7784), pp.647-651.

O'Neill, B. C., Tebaldi, C., van Vuuren, D. P., Eyring, V., Friedlingstein, P., Hurtt, G., et al. (2016). The Scenario Model Intercomparison Project (ScenarioMIP) for CMIP6. Geoscientific Model Development, 9(9), 3461–3482. https://doi.org/10.5194/gmd-9-3461-2016

Perry, S. J., S. McGregor, A. Sen Gupta, and M. H. England, 2017: Future Changes to El Niño–Southern Oscillation Temperature and Precipitation Teleconnections. Geophys. Res. Lett., 44, 10,608-10,616, https://doi.org/10.1002/2017GL074509.

Pillai, P.A., Nair, R.C. and Vidhya, C.V., 2019. Recent changes in the prominent modes of Indian Ocean dipole in response to the tropical Pacific Ocean SST patterns. Theoretical and Applied Climatology, 138, pp.941-951.

Saji, N.H., Goswami, B.N., Vinayachandran, P.N. and Yamagata, T., 1999. A dipole mode in the tropical Indian Ocean. Nature, 401(6751), pp.360-363.

Saji, N.H. and Yamagata, T., 2003. Structure of SST and surface wind variability during Indian Ocean dipole mode events: COADS observations. Journal of Climate, 16(16), pp.2735-2751.

Schott, F.A., Xie, S.P. and McCreary Jr, J.P., 2009. Indian Ocean circulation and climate variability. Reviews of Geophysics, 47(1).

S. C. Sherwood, M. J. Webb, J. D. Annan, K. C. Armour, P. M. Forster, J. C. Hargreaves, G. Hegerl, S. A. Klein, K. D. Marvel, E. J. Rohling, M. Watanabe, T. Andrews, P. Braconnot, C. S. Bretherton, G. L. Foster, Z. Hausfather, A. S. von der Heydt, R. Knutti, T. Mauritsen, J. R. Norris, C. Proistosescu, M. Rugenstein, G. A. Schmidt, K. B. Tokarska, M. D. Zelinka, 2020. An Assessment of Earth's Climate Sensitivity Using Multiple Lines of Evidence. Reviews of Geophysics, DOI:10.1029/2019RG000678.

Stuecker, M.F., Timmermann, A., Jin, F.F., Chikamoto, Y., Zhang, W., Wittenberg, A.T., Widiasih, E. and Zhao, S., 2017. Revisiting ENSO/Indian Ocean dipole phase relationships. Geophysical Research Letters, 44(5), pp.2481-2492.

Stuecker, M. F., F. F. Jin, A. Timmermann, and S. Mcgregor, 2015: Combination mode dynamics of the anomalous northwest pacific anticyclone. J. Clim., 28, 1093–1111, https://doi.org/10.1175/JCLI-D-14-00225.1.

Taschetto, A. S., C. C. Ummenhofer, M. F. Stuecker, D. Dommenget, K. Ashok, R. R. Rodrigues, and S. Yeh, 2020: ENSO Atmospheric Teleconnections. 309–335.

Wang, B., R. Wu, and T. Li, 2003: Atmosphere-warm ocean interaction and its impacts on Asian-Australian monsoon variation. J. Clim., 16, 1195–1211, https://doi.org/10.1175/1520-0442(2003)16<1195:AOIAII>2.0.CO;2.

Wang, J., DeFlorio, M.J., Kim, H., Guirguis, K. and Gershunov, A., 2023. CMIP6 projections of future MJO changes under steepened moisture gradient conditions over the Indo-Pacific warm pool. Authorea Preprints.

Wheeler, M.C., Kim, H.J., Lee, J.Y. and Gottschalck, J.C., 2017. Real-time forecasting of modes of tropical intraseasonal variability: The Madden-Julian and boreal summer intraseasonal oscillations. In The Global Monsoon System: Research and Forecast (pp. 131-138).

Wolding, B.O., Maloney, E.D., Henderson, S. and Branson, M., 2017. Climate change and the Madden-Julian Oscillation: A vertically resolved weak temperature gradient analysis. Journal of Advances in Modeling Earth Systems, 9(1), pp.307-331.

Yan, Z., B. Wu, T. Li, M. Collins, R. Clark, T. Zhou, J. Murphy, and G. Tan, 2020: Eastward shift and extension of ENSO-induced tropical precipitation anomalies under global warming. 1–11.

Yeh, S. W., and Coauthors, 2018: ENSO Atmospheric Teleconnections and Their Response to Greenhouse Gas Forcing. Rev. Geophys., 56, 185–206, https://doi.org/10.1002/2017RG000568.

Zelinka, M. D., Myers, T. A., McCoy, D. T., Po-Chedley, S., Caldwell, P. M., Ceppi, P., et al. (2020). Causes of Higher Climate Sensitivity in CMIP6 Models. Geophysical Research Letters, 47(1), e2019GL085782. https://doi.org/10.1029/2019GL085782

Zhang, C., 2005. Madden-julian oscillation. Reviews of Geophysics, 43(2).

Eyring, V., Bony, S., Meehl, G. A., Senior, C. A., Stevens, B., Stouffer, R. J., & Taylor, K. E. (2016). Overview of the Coupled Model Intercomparison Project Phase 6 (CMIP6) experimental design and organization. Geoscientific Model Development, 9(5), 1937–1958. https://doi.org/10.5194/gmd-9-1937-2016.